Journal of Applied Physics

Dynamic adhesion of 2D materials to mixed-phase $BiFeO_3$ structural phase transitions

Cite as: J. Appl. Phys. **132**, 045301 (2022); https://doi.org/10.1063/5.0096686
Submitted: 20 April 2022 • Accepted: 01 July 2022 • Published Online: 22 July 2022

Carla Watson, Tara Peña, Marah Abdin, et al.

Journal of Applied Physics ARTICLE scitation.org/journal/jap

Dynamic adhesion of 2D materials to mixed-phase $BiFeO_3$ structural phase transitions

Cite as: J. Appl. Phys. **132**, 045301 (2022); doi: 10.1063/5.0096686
Submitted: 20 April 2022 · Accepted: 1 July 2022 ·
Published Online: 22 July 2022

Carla Watson,[1] Tara Peña,[2] Marah Abdin,[2] Tasneem Khan,[2] and Stephen M. Wu[1,2,a)]

AFFILIATIONS

[1]Department of Physics and Astronomy, University of Rochester, Rochester, New York 14627, USA
[2]Department of Electrical and Computer Engineering, University of Rochester, Rochester, New York 14627, USA

[a)]**Author to whom correspondence should be addressed:** stephen.wu@rochester.edu

ABSTRACT

Two-dimensional materials, such as transition metal dichalcogenides, have generated much interest due to their strain-sensitive electronic, optical, magnetic, superconducting, or topological properties. Harnessing control over their strain state may enable new technologies that operate by controlling these materials' properties in devices such as straintronic transistors. Piezoelectric oxides have been proposed as one method to control such strain states on the device scale. However, there are few studies of how conformal 2D materials remain on oxide materials with respect to dynamic applications of the strain. Non-conformality may lead to non-optimal strain transfer. In this work, we explore this aspect of oxide-2D adhesion in the nanoscale switching of the substrate structural phase in thin 1T′-$MoTe_2$ attached to a mixed-phase thin-film $BiFeO_3$ (BFO), a multiferroic oxide with an electric-field induced structural phase transition that can generate mechanical strains of up to 2%. We observe that flake thickness impacts the conformality of 1T′-$MoTe_2$ to structural changes in BFO, but below four layers, 1T′-$MoTe_2$ fully conforms to the nanoscale BFO structural changes. The conformality of few-layer 1T′-$MoTe_2$ suggests that BFO is an excellent candidate for deterministic, nanoscale strain control for 2D materials.

I. INTRODUCTION

Two-dimensional transition metal dichalcogenides (2D-TMDCs) are atomically thin materials that have been proposed for numerous nanoelectronic and optoelectronic applications. Of particular interest are TMDCs that possess strain-sensitive materials properties, such as strain-tuned bandgap modulation,[1–3] strain-sensitive superconductivity,[4,5] and strain-mediated control over topological insulating states.[6] Controlling strain in TMDCs could expand the capabilities of existing electronic, optoelectronic, or quantum electronic device technologies by allowing for direct dynamic control over these parameters. This is the focus of straintronic devices, which use strain applied at the device level as another degree of freedom to tune and control materials in applications.

Many different methods to control strain in 2D materials have been implemented.[7] Examples include controlled wrinkling or buckling,[8–10] exfoliating 2D materials onto bendable flexible substrates,[1,11,12] inducing bubbles with differential pressure,[13,14] applying force from scanning probe tips,[15–18] using microelectromechanical devices (MEMS),[19–21] and through applying gate-controllable strain through the use of piezoelectric dielectrics.[22–24] Each technique has its unique advantages and disadvantages, but for straintronic devices, we desire a method to apply large-magnitude electric-field controllable nanoscale strain in a scalable device structure. One of the few methods to do this is through the use of piezoelectrics, taking advantage of the converse piezoelectric effect to generate mechanical strain in well-adhered 2D materials. Relaxor ferroelectric oxides have large piezoelectric constants, and in systems such as $Pb(Mg_{1/3}Nb_{2/3})_{0.71}Ti_{0.29}O_3$ (PMN-PT), they can generate up to 0.2% dynamic strain controllable by applied electric-field across the oxide. This has been successfully used to tune the bandgaps in both tri-layer MoS_2 and α-In_2Se_3.[22,23] In our own previous work, we were able to use this effect in PMN-PT to control a semimetallic to semi-conducting phase transition in 1T′-$MoTe_2$.[24]

One disadvantage of using piezoelectrics is that the magnitude of dynamic strain control in these systems is small, and at the nanoscale, it is not clear how adhesion plays a role in effective strain transfer in these oxide-2D systems. To solve the strain magnitude problem, we explore the use of thin-film multi-phase $BiFeO_3$ (BFO), which has a reversible non-volatile electric-field

controllable structural phase transition between its rhombohedral (R) and tetragonal (T) phases. Using this effect, it is possible to transfer up to 2% strain[25] into adhered 2D material layers in a similar method to our piezoelectric-based straintronic devices. In this way, we may be able to surpass the level of dynamically controllable strain in conventional piezoelectrics by an order of magnitude.

In this work, we examine the one remaining issue in implementing BFO-based straintronic devices, the role of 2D flake thickness and oxide surface roughness to how well 2D layers adhere to the BFO surface for effective strain transfer. It is well known that on corrugated surfaces, exfoliated 2D materials such as graphene exhibit a thickness-dependent "snap-through" transition due to competition between the bending energy of the 2D membrane and its adhesion energy to the substrate.[26] Above the critical "snap-through" thickness, bending energy exceeds the adhesion energy and 2D membranes lie flat atop the corrugated surface. Below a critical thickness, the 2D membranes conform to the corrugation and experiences substrate-induced strain transfer. We apply this same idea to explore coherent conformality in exfoliated 1T′-$MoTe_2$ on BFO under *dynamic* changes to substrate corrugation caused by BFO structural phase transformations [Fig. 1(a), left]. While this snap-through transition has been well explored in static systems,[26–31] the dynamic nature of this transition has not yet been explored but is critical for the implementation of oxide-based straintronic devices.

We choose to explore these concepts on 1T′-$MoTe_2$ because it is an important system that hosts the potential for strain controllable structural/electronic phases,[32,33] strain controllable superconductivity,[4,5,34] and strain-mediated topological phase transitions between its Weyl semimetallic states.[35,36] By examining the conformality of the exfoliated $MoTe_2$ flakes with respect to structural changes in BFO, we can judge the thickness limit of coherent adhesion under BFO structural phase transformation for this particular 2D material. We find that 1T′-$MoTe_2$ conforms to the structural changes in BFO with varying degrees of conformality with respect to thickness: full conformality, partial conformality, and no conformality [Fig. 1(a), right]. To fully confer the maximal strain from BFO to the 2D material, we must ensure full conformality.

II. METHODS AND MATERIALS

The outline of our experimental technique is shown in Fig. 1(a), where 1T′-$MoTe_2$ is directly exfoliated onto thin-film BFO, grown with a thin conducting $La_{0.7}Sr_{0.3}MnO_3$ (LSMO) counterelectrode layer underneath. We start with regions of $MoTe_2$ exfoliated onto the purely tetragonal phase of BFO to ensure the highest level of starting conformality and adhesion. By applying a positive electric bias with a conducting atomic force microscope (C-AFM) probe, we can transform flat T-BFO regions into corrugated mixed R- and T-phase regions. We then study conformability between 1T′-$MoTe_2$ and these non-volatile BFO transformations by correlating topographic changes obtained by atomic force microscopy (AFM) to conformability. The different crystalline polymorphs of BFO are readily apparent under AFM analysis with

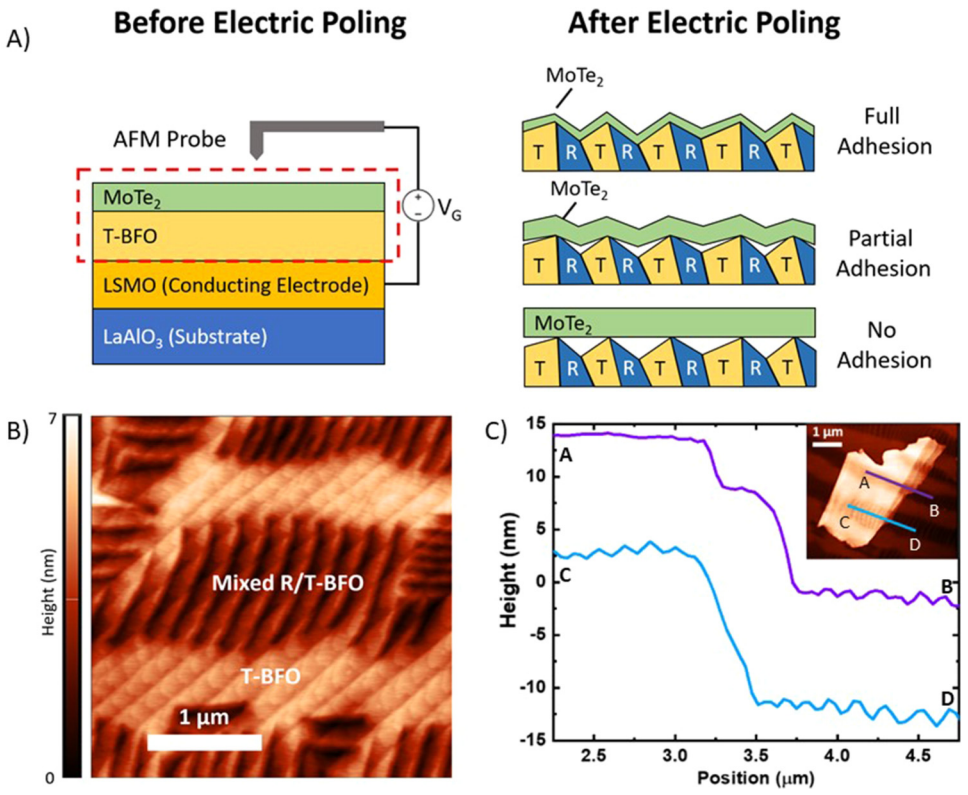

FIG. 1. Schematic of conducting atomic force microscopy-based electric-poling process to induce non-volatile structural transformations in BFO and $MoTe_2$. (a) Diagrams for $MoTe_2$ possible adhesion cases after electric-field induced structural phase transformations of the highlighted region. (b) AFM of the mixed-phase BFO/LSMO/LAO substrate surface prior to the transfer of $MoTe_2$. (c) Height profile of non-adhered (purple) and adhered (blue) $MoTe_2$ exfoliated on BFO in regions indicated on the inset.

approximately 2 nm deep corrugations corresponding to mixed R/T-phase BFO domains [Fig. 1(b)]. Sufficiently conformal flakes also exhibit these corrugations. In Fig. 1(c), a flake with varying conformality has a relatively smooth surface in the nonconformal region. In the conformal region, the flake has corrugations of similar periodicity and amplitude (position C) to those on bare BFO (position D). These measurable differences in conformality form the basis of our analysis in this paper.

To fabricate the BFO/LSMO/$LaAlO_3$ (100) heterostructures, we employed 90° off-axis RF magnetron sputtering. Cleaved, single-side polished $LaAlO_3$ (LAO) (100) were cleaned via sonication for 30 min in acetone and 30 min in isopropyl alcohol and then dried with compressed nitrogen. The crystals were affixed to the sputtering heating stage with silver paste. Within the sputtering chamber, substrates were pre-baked for 30 min at 300 °C under a vacuum pressure of $\sim 10^{-8}$ Torr. LSMO was sputtered at 700 °C for 5 min with an Ar flow rate of 50 SCCM, an O_2 flow rate of 2 SCCM, and a total pressure of 11 mTorr. Afterward, BFO was sputtered at 750 °C for 90 min with an Ar flow rate of 50 SCCM, an O_2 flow rate of 4 SCCM, and a total pressure of 11 mTorr. This process yielded substrates BFO/LSMO/LAO(100) with a ~160 nm layer of BFO and an ~2–3 nm layer of LSMO as measured via profilometry and atomic force microscopy (AFM). Growth quality and phase purity were examined via x-ray diffractometry (XRD). Figure 1(b) demonstrates the quality of the oxide thin-film growth process through an atomic force micrograph of a typical BFO/LSMO/LAO heterostructure, which shows clearly identifiable mixed-phase regions,[25] along with atomic scale terraces associated with layer-by-layer Frank-van der Merwe growth modes. This level of oxide heterostructure atomic smoothness is required for our analysis of 2D adhesion and subsequent understanding of how dynamic structure phase changes may affect 2D conformality.

Thin 1T′-$MoTe_2$ flakes were cleaved from bulk 1T′-$MoTe_2$ crystals from HQ graphene via mechanical exfoliation with low-residue tape inside a low-oxygen and humidity-controlled glovebox (<0.5 ppm O_2 and H_2O). BFO/LSMO/LAO samples were pre-annealed at 100 °C inside the glovebox for 30 min, prior to exfoliation to promote adhesion because this has been shown to remove adsorbates from the oxide surface.[37] Using the tape, 1T′-$MoTe_2$ crystals were directly exfoliated onto mixed-phase BFO/LSMO/LAO (100) and annealed for 3 min at 100 °C to further promote adhesion prior to tape removal. Flake thicknesses were identified via optical contrast measurements in an optical microscope and verified through AFM measurements. It is observed that in the static case after exfoliation conformality varies across the sample in the mixed-phase regions, as seen in Fig. 1(c), which is consistent with other experimental and theoretical works on *static* 2D conformality to corrugated substrates.[30,31] The degree of conformality in the static case can be modeled knowing 2D flake bending stiffness, 2D adhesion, corrugation amplitude, and corrugation wavelength[26,38,39] using energy minimization methods. Here, we seek to further examine how adhesion may change in these systems in the case of *dynamic* changes to substrate corrugation, a prerequisite for using BFO to drive electric-field controllable dynamic strain into the 2D systems.

To explore whether these same factors play a role in 2D flake conformality in the dynamic case, we start with a fully adhered $MoTe_2$ flake on a flat T-BFO region. Electric-field induced structural phase transitions in BFO/LSMO/LAO(100) were performed via conducting atomic force microscopy (C-AFM). A low-force 6 N/m spring constant conducting diamond-coated AFM probe (Bruker DDESP-FM-V2) was employed to minimize damage while poling the flake and the substrate. The conducting LSMO layer was grounded while a +8 V bias was applied to the conducting probe to generate an electric-field in the BFO layer, triggering the T to R-BFO transition. Root mean square surface roughness (R_q) measurements were averaged from multiple AFM line profiles over $MoTe_2$ and BFO surfaces that experienced non-volatile changes from fully T to mixed R/T regions before and after the electric-poling process.

III. RESULTS AND DISCUSSION

As a control, electric-poling measurements were initially carried out on bare BFO/LSMO/LAO(100) via C-AFM to induce non-volatile structural T- to R/T-phase transitions in BFO. As shown in Figs. 2(a) and 2(b), these transformations are readily apparent as the appearance of new stripes—approximately 2 nm in amplitude appearing in the formerly T-phase regions—corresponding to the non-volatile changes of BFO from the T to the mixed T/R-BFO structural phases. Next, thin 1T′-$MoTe_2$ flakes were transferred to fresh BFO/LSMO/LAO(100) substrates, and the electric-poling process was repeated. In Figs. 2(c)–2(f), it is possible to resolve the underlying corrugation induced by the non-volatile BFO phase switching through the 1T′-$MoTe_2$ flakes, but this varies as a function of flake thickness. The 5 nm thick 1T′-$MoTe_2$ flake was highly conformal to the electric-field induced R/T corrugations [Figs. 2(c) and 2(d)], while the 18.5 nm flake was partially conformal with new corrugations appearing in the upper half of the flake [Figs. 2(e) and 2(f)]. The 78 nm $MoTe_2$ flake does not display any underlying corrugation despite the structural transformation of the surrounding BFO [Figs. 2(g) and 2(h)]. We note that instrumental limitations are not the reason that the corrugations are not resolvable for thicker flakes since we can resolve corrugations in Ni electrodes and other materials of similar thickness (Fig. S1 in the supplementary material).

To verify that the non-volatile changes are not induced via pressure from the AFM probe itself, a series of contact-mode AFM measurements were performed under varying tip pressures (Fig. 3). When the tip pressure was increased to 4× the typical magnitude used in electric-poling measurements [Fig. 3(b)], the $MoTe_2$ flake and BFO surface remained unchanged [Fig. 3(c)]. Based on these results, we expect that topographic changes in flakes occur primarily due to the electric-field induced structural transitions in the underlying BFO instead of tip pressure.

To measure the impact of flake thickness on flake conformability, 1T′-$MoTe_2$ flakes between 3 and 78 nm in thickness were exfoliated onto our BFO substrates, then electrically poled via C-AFM. Surface roughness amplitude ratios corresponding to surface roughness changes on the 1T′-$MoTe_2$ before and after electric poling were used as a metric for flake conformability. Root mean square (RMS) surface roughness measurements were performed on $MoTe_2$ flakes before electric poling (R_{before}) and after electric poling (R_{after}).

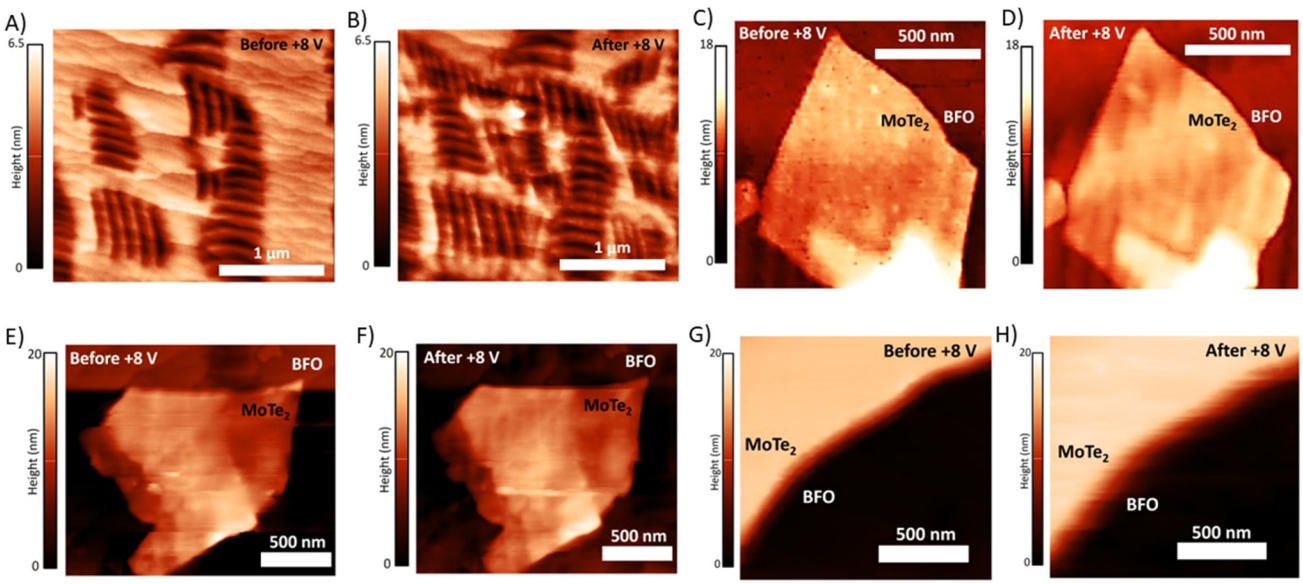

FIG. 2. Atomic force microscope images of non-volatile electric-field induced transformation on BFO and $MoTe_2$/BFO. (a) and (b) Mixed-phase BFO/LSMO/LAO heterostructure without $MoTe_2$ before and after poling, showing electric-field controllable structural phase transitions. (c) and (d) 5 nm, (e) and (f) 18.5 nm, and (g) and (h) 78 nm of $MoTe_2$ on BFO/LSMO/LAO before and after poling, showing full non-volatile conformality in (d), partial conformality in (f), and no conformality in (h).

After extracting surface profiles, the RMS roughness of a given line profile can be calculated as follows, where R_q is the RMS roughness, l_r is the length of the line profile, and $Z(x)$ is the height at location x,

$$R_q = \sqrt{\frac{1}{l_r}\int_0^{l_r} Z^2(x)dx}\,. \tag{1}$$

In this experiment, we define the amplitude ratio $A = R_{after}/R_{before}$ as a measure of 1T′-$MoTe_2$ flake conformality to non-volatile BFO corrugations induced by the electric-poling process, where R_{before} is the surface roughness of a flake region on top of the relatively flat T-BFO domains and R_{after} is the surface roughness of the same flake region on top of new corrugated mixed R/T-BFO domains. Similar measurements were repeated on bare BFO to define $A_{max} = R_{BFO,after}/R_{BFO,before}$, corresponding to the maximal possible amplitude ratio and maximal conformality. In Fig. 4, the region of maximal conformality is highlighted in orange, spanning one standard deviation below and above A_{max}. The surface roughness amplitude A decays with 1T′-$MoTe_2$ flake thickness with an exponential decay length scale of 6.4 ± 1.0 nm. Because monolayer 1T′-$MoTe_2$ is 0.82 nm thick[40] and the fitted curve intersects the maximal conformality region at approximately 3.2 nm, we expect that flakes of four layers or less should fully conform to the BFO transformations. Based on these results, the flakes of up to at least 20 nm in thickness may be partially conformal to the BFO substrate with little or no conformality beyond.

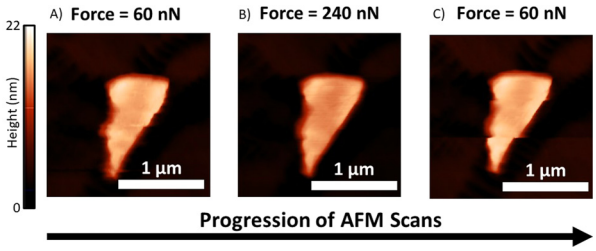

FIG. 3. Series of successive AFM measurements performed on a 20 nm thick flake of $MoTe_2$ with varying probe pressure. (a) Initial scan with a probe force of 60 nN. (b) Intermediate scan with a probe force of 240 nN. (c) Final scan returning to original probe force of 60 nN.

Using measurable material parameters such as 1T′-$MoTe_2$ flake thickness, bending stiffness, corrugation amplitudes and wavelengths, and adhesion energies, conformability of the 2D materials may be studied via classical methods: continuum models[41] and energy minimization methods[39,42] have been used to study thin and flexible materials such as graphene with some success. However, preliminary efforts to model with an energy minimization method[39] in our system could not reproduce the partial conformability of $MoTe_2$. This may be because the bending rigidity of van der Waals (vdW) type materials depart from the classical model of an elastic plate due to the weak inter-layer bonds in multilayer 2D materials and may be affected by inter-layer shear effects.[43] Atomistic models such as molecular dynamics may better approximate the effects of vdW interactions in 2D materials and have found success in modeling the adhesion of graphene[44] and MoS_2.[45] Further works on modeling dynamic strain and adhesion

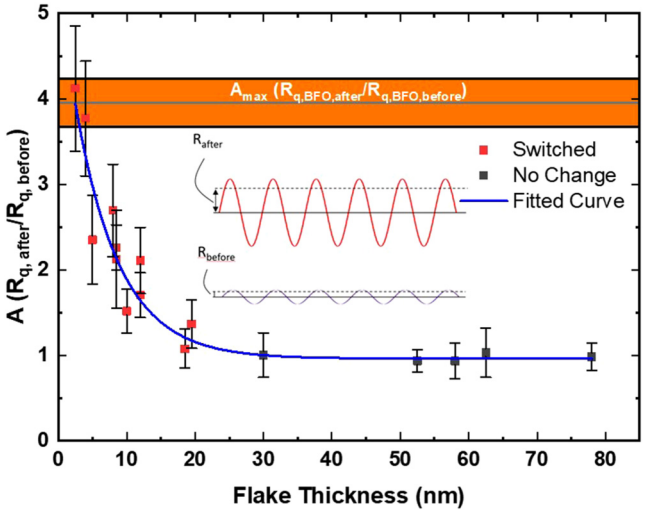

FIG. 4. Comparison of RMS roughness amplitude before and after electric-field induced structural phase transitions with varying $MoTe_2$ flake thickness. The inset illustrates RMS surface roughness measurements calculated from the line profiles. Points and error bars were calculated based on statistical averages and standard deviations of RMS surface roughness from multiple line scans on flake surfaces surrounding structurally transformed areas. The orange region corresponds to two standard deviations of the mean RMS amplitude ratios of bare BFO in structurally transformed regions.

processes in this system are necessary to clarify the role of membrane thickness in our empirical result.

IV. CONCLUSIONS

We have studied the variations of conformality in electrically poled 1T′-$MoTe_2$ flakes of various thicknesses that have been transferred to BFO/LSMO/LAO(100). The application of an out-of-plane electric-field to the 1T′-$MoTe_2$/BFO stack triggers a structural phase transition from T to R-BFO, resulting in corrugations due to mixed R/T-BFO domains. Depending on the thickness of 1T′-$MoTe_2$, flakes either fully conform, partially conform, or do not conform to the R/T-BFO corrugations due to competition between the flake bending stiffness and substrate adhesion energies. Based on the surface roughness amplitude ratios corresponding to the roughness amplitudes before and after the induction of the BFO phase transitions, four-layer 1T′-$MoTe_2$ is fully conformal to the non-volatile changes in corrugation. Ensuring the conformality of 2D materials such as 1T′-$MoTe_2$ is essential for deterministic control over the strain state in 2D crystals. The observed conformality of few-layer 1T′-$MoTe_2$ suggests that BFO-based straintronic platforms may be suitable for controlling large strain magnitudes of 2% down to the nanoscale.

SUPPLEMENTARY MATERIAL

See the supplementary material for a comparison of AFM characterization of Ni electrodes fabricated on mixed-phase BFO substrate to 1T′-$MoTe_2$ transferred to mixed-phase BFO.

ACKNOWLEDGMENTS

We acknowledge our support from the National Science Foundation (NSF) (Nos. OMA-1936250 and ECCS-1942815) and the National Science Foundation Graduate Research Fellowship Program (No. DGE-1939268).

AUTHOR DECLARATIONS

Conflict of Interest

The authors have no conflicts to disclose.

Author Contributions

Carla Watson: Conceptualization (equal); Data curation (equal); Formal analysis (equal); Investigation (equal); Methodology (equal); Visualization (equal); Writing – original draft (equal); Writing – review and editing (equal). **Tara Peña:** Investigation (equal). **Marah Abdin:** Investigation (equal). **Tasneem Khan:** Investigation (equal). **Stephen M. Wu:** Conceptualization (equal); Funding acquisition (equal); Investigation (equal); Project administration (equal); Resources (equal); Supervision (equal); Validation (equal); Writing – original draft (equal); Writing – review and editing (equal).

DATA AVAILABILITY

The data that support the findings of this study are available from the corresponding author upon reasonable request.

REFERENCES

[1]H. J. Conley, B. Wang, J. I. Ziegler, R. F. Haglund, S. T. Pantelides, and K. I. Bolotin, Nano Lett. **13**, 3626 (2013).
[2]Y. Wang, C. Cong, W. Yang, J. Shang, N. Peimyoo, Y. Chen, J. Kang, J. Wang, W. Huang, and T. Yu, Nano Res. **8**, 2562 (2015).
[3]R. Schmidt, I. Niehues, R. Schneider, M. Drüppel, T. Deilmann, M. Rohlfing, S. M. de Vasconcellos, A. Castellanos-Gomez, and R. Bratschitsch, 2D Mater. **3**, 021011 (2016).
[4]C. Heikes, I.-L. Liu, T. Metz, C. Eckberg, P. Neves, Y. Wu, L. Hung, P. Piccoli, H. Cao, J. Leao, J. Paglione, T. Yildirim, N. P. Butch, and W. Ratcliff, Phys. Rev. Mater. **2**, 074202 (2018).
[5]D. A. Rhodes, A. Jindal, N. F. Q. Yuan, Y. Jung, A. Antony, H. Wang, B. Kim, Y. Chiu, T. Taniguchi, K. Watanabe, K. Barmak, L. Balicas, C. R. Dean, X. Qian, L. Fu, A. N. Pasupathy, and J. Hone, Nano Lett. **21**, 2505 (2021).
[6]H. Xiang, B. Xu, J. Liu, Y. Xia, H. Lu, J. Yin, and Z. Liu, AIP Adv. **6**, 095005 (2016).
[7]Z. Peng, X. Chen, Y. Fan, D. J. Srolovitz, and D. Lei, Light Sci. Appl. **9**, 190 (2020).
[8]L. Meng, Y. Su, D. Geng, G. Yu, Y. Liu, R.-F. Dou, J.-C. Nie, and L. He, Appl. Phys. Lett. **103**, 251610 (2013).
[9]M. G. Pastore Carbone, A. C. Manikas, I. Souli, C. Pavlou, and C. Galiotis, Nat. Commun. **10**, 1572 (2019).
[10]Z. Li, R. J. Young, D. G. Papageorgiou, I. A. Kinloch, X. Zhao, C. Yang, and S. Hao, 2D Mater. **6**, 045026 (2019).
[11]J. O. Island, A. Kuc, E. H. Diependaal, R. Bratschitsch, H. S. J. van der Zant, T. Heine, and A. Castellanos-Gomez, Nanoscale **8**, 2589 (2016).
[12]Z. Li, Y. Lv, L. Ren, J. Li, L. Kong, Y. Zeng, Q. Tao, R. Wu, H. Ma, B. Zhao, D. Wang, W. Dang, K. Chen, L. Liao, X. Duan, X. Duan, and Y. Liu, Nat. Commun. **11**, 1151 (2020).
[13]N. Levy, S. A. Burke, K. L. Meaker, M. Panlasigui, A. Zettl, F. Guinea, A. H. C. Neto, and M. F. Crommie, Science **329**, 544 (2010).

[14]J. Pető, G. Dobrik, G. Kukucska, P. Vancsó, A. A. Koós, J. Koltai, P. Nemes-Incze, C. Hwang, and L. Tapasztó, npj 2D Mater. Appl. **3**, 1 (2019).
[15]J. Qi, Y.-W. Lan, A. Z. Stieg, J.-H. Chen, Y.-L. Zhong, L.-J. Li, C.-D. Chen, Y. Zhang, and K. L. Wang, Nat. Commun. **6**, 7430 (2015).
[16]K. Elibol, B. C. Bayer, S. Hummel, J. Kotakoski, G. Argentero, and J. C. Meyer, Sci. Rep. **6**, 28485 (2016).
[17]Y. Sun, J. Pan, Z. Zhang, K. Zhang, J. Liang, W. Wang, Z. Yuan, Y. Hao, B. Wang, J. Wang, Y. Wu, J. Zheng, L. Jiao, S. Zhou, K. Liu, C. Cheng, W. Duan, Y. Xu, Q. Yan, and K. Liu, Nano Lett. **19**, 761 (2019).
[18]B. Lyu, H. Li, L. Jiang, W. Shan, C. Hu, A. Deng, Z. Ying, L. Wang, Y. Zhang, H. A. Bechtel, M. C. Martin, T. Taniguchi, K. Watanabe, W. Luo, F. Wang, and Z. Shi, Nano Lett. **19**, 1982 (2019).
[19]H. H. Pérez Garza, E. W. Kievit, G. F. Schneider, and U. Staufer, Nano Lett. **14**, 4107 (2014).
[20]M. Goldsche, J. Sonntag, T. Khodkov, G. J. Verbiest, S. Reichardt, C. Neumann, T. Ouaj, N. von den Driesch, D. Buca, and C. Stampfer, Nano Lett. **18**, 1707 (2018).
[21]J. W. Christopher, M. Vutukuru, D. Lloyd, J. S. Bunch, B. B. Goldberg, D. J. Bishop, and A. K. Swan, J. Microelectromech. Syst. **28**, 254 (2019).
[22]Y. Y. Hui, X. Liu, W. Jie, N. Y. Chan, J. Hao, Y.-T. Hsu, L.-J. Li, W. Guo, and S. P. Lau, ACS Nano **7**, 7126 (2013).
[23]F. Guo, Y. Lyu, M. B. Jedrzejczyk, Y. Zhao, W. F. Io, G. Bai, W. Wu, and J. Hao, Appl. Phys. Lett. **116**, 113101 (2020).
[24]W. Hou, A. Azizimanesh, A. Sewaket, T. Peña, C. Watson, M. Liu, H. Askari, and S. M. Wu, Nat. Nanotechnol. **14**, 668 (2019).
[25]R. J. Zeches, M. D. Rossell, J. X. Zhang, A. J. Hatt, Q. He, C.-H. Yang, A. Kumar, C. H. Wang, A. Melville, C. Adamo, G. Sheng, Y.-H. Chu, J. F. Ihlefeld, R. Erni, C. Ederer, V. Gopalan, L. Q. Chen, D. G. Schlom, N. A. Spaldin, L. W. Martin, and R. Ramesh, Science **326**, 977 (2009).
[26]T. Li and Z. Zhang, Nanoscale Res. Lett. **5**, 169 (2010).
[27]T. Li and Z. Zhang, J. Phys. D: Appl. Phys. **43**, 075303 (2010).
[28]S. Viola Kusminskiy, D. K. Campbell, A. H. Castro Neto, and F. Guinea, Phys. Rev. B **83**, 165405 (2011).
[29]Z. Zhang and T. Li, J. Appl. Phys. **110**, 083526 (2011).
[30]S. Scharfenberg, D. Z. Rocklin, C. Chialvo, R. L. Weaver, P. M. Goldbart, and N. Mason, Appl. Phys. Lett. **98**, 091908 (2011).
[31]S. Scharfenberg, N. Mansukhani, C. Chialvo, R. L. Weaver, and N. Mason, Appl. Phys. Lett. **100**, 021910 (2012).
[32]K.-A. N. Duerloo, Y. Li, and E. J. Reed, Nat. Commun. **5**, 4214 (2014).
[33]S. Song, D. H. Keum, S. Cho, D. Perello, Y. Kim, and Y. H. Lee, Nano Lett. **16**, 188 (2016).
[34]Y. Qi, P. G. Naumov, M. N. Ali, C. R. Rajamathi, W. Schnelle, O. Barkalov, M. Hanfland, S.-C. Wu, C. Shekhar, Y. Sun, V. Süß, M. Schmidt, U. Schwarz, E. Pippel, P. Werner, R. Hillebrand, T. Förster, E. Kampert, S. Parkin, R. J. Cava, C. Felser, B. Yan, and S. A. Medvedev, Nat. Commun. **7**, 11038 (2016).
[35]Y. Sun, S.-C. Wu, M. N. Ali, C. Felser, and B. Yan, Phys. Rev. B **92**, 161107 (2015).
[36]Z. Wang, D. Gresch, A. A. Soluyanov, W. Xie, S. Kushwaha, X. Dai, M. Troyer, R. J. Cava, and B. A. Bernevig, Phys. Rev. Lett. **117**, 056805 (2016).
[37]J. H. Linn and W. E. Swartz, Appl. Surface Sci. **20**, 154 (1984).
[38]S. Qiao, J.-B. Gratadour, L. Wang, and N. Lu, IEEE Trans. Compon. Packag. Manuf. Technol. **5**, 1237 (2015).
[39]L. Wang and N. Lu, J. Appl. Mech **83**, 041007 (2016).
[40]S. Pace, L. Martini, D. Convertino, D. H. Keum, S. Forti, S. Pezzini, F. Fabbri, V. Mišeikis, and C. Coletti, ACS Nano **15**, 4213 (2021).
[41]M. Poot and H. S. J. van der Zant, Appl. Phys. Lett. **92**, 063111 (2008).
[42]W. Gao and R. Huang, J. Phys. D: Appl. Phys. **44**, 452001 (2011).
[43]G. Wang, Z. Dai, J. Xiao, S. Feng, C. Weng, L. Liu, Z. Xu, R. Huang, and Z. Zhang, Phys. Rev. Lett. **123**, 116101 (2019).
[44]H. Chen, Y. Yao, and S. Chen, J. Phys. D: Appl. Phys. **46**, 205303 (2013).
[45]Y. Hu, F. Zhang, M. Titze, B. Deng, H. Li, and G. J. Cheng, Nanoscale **10**, 5717 (2018).